Journal of the Mechanics and Physics of Solids 58 (2010) 129–144

Contents lists available at ScienceDirect

Journal of the Mechanics and Physics of Solids

journal homepage: www.elsevier.com/locate/jmps

Discrete element modelling of pebble beds: With application to uniaxial compression tests of ceramic breeder pebble beds

Yixiang Gan *, Marc Kamlah

Institute for Materials Research II (IMF II), Karlsruhe Institute of Technology (KIT), D-76344 Eggenstein-Leopoldshafen, Germany

ARTICLE INFO

Article history:
Received 21 November 2008
Received in revised form
20 October 2009
Accepted 24 October 2009

Keywords:
Discrete element method
Pebble beds
Numerical simulation
Constitutive behaviour
Force chains

ABSTRACT

In this paper, a discrete element simulation scheme for pebble beds in fusion blankets is presented. Each individual pebble is considered as one element obeying equilibrium conditions under contact forces. We study not only the rearrangement of particles but also the overall behaviour of an assembly under the action of macroscopic compressive stresses. Using random close packing as initial configurations, the discrete element simulation of the uniaxial compression test has been quantitatively compared to experiments. This method yields the distribution of the inter-particle contact forces. Moreover, the micro–macro relations have been investigated to relate the microscopic information, such as the maximum contact force and the coordination number inside the assembly, to the macroscopic stress variables.

1. Introduction

Nuclear fusion provides a promising and sustainable solution for the future energy demand, in particular the electricity demand, without long-term radioactive waste and greenhouse gas emission. Working as tritium breeder and neutron multiplier in fusion reactors, lithium-based ceramic, such as Li_4SiO_4 (Knitter et al., 2007), and beryllium pebble beds, respectively, are under severe thermo-mechanical loads (Reimann et al., 2002). Thus, the thermo-mechanics of these materials being composed of nearly spherically shaped particles is not only essential to understand the behaviour due to external excitations, but also important for the design, characterization and diagnostics of components in fusion blankets.

Similar to sand and soil, pebble beds can be modelled by either a discrete element method (An et al., 2007a, b) or a continuum approach (Gan and Kamlah, 2007). The first approach is usually used to investigate the physics behind the macroscopic behaviour of the material, and the second one is practical in engineering applications, such as fully coupled thermo-mechanical analyses of structures containing pebble beds. The aim of both approaches is to represent the constitutive behaviour of the material in the framework of different models. The agreement between predictions of models and experimental results, such as the uniaxial compression test, is the key to show the applicability of material models. Besides the similarities to the plastic behaviour of metals, namely, nearly rate-independent plastic deformation and yield stress, granular materials have relatively strong dependence on pressure and volume changes. Increasing the hydrostatic pressure on a granular material can introduce further irreversible deformation which can be accompanied by a reduction in volume. The changes in volume can either harden or soften the material assemblies. Another common feature of granular materials is the dilatancy under shear stresses. When sheared, the interlocking particles in a compacted state move and produce a bulk expansion of the material. The overall plastic deformation of pebble beds results from a combination of the

* Corresponding author. Tel.: +49 7247 823459; fax: +49 7247 822347.
E-mail address: yixiang.gan@kit.edu (Y. Gan).

0022-5096/$ - see front matter © 2009 Published by Elsevier B.V.
doi:10.1016/j.jmps.2009.10.009

plastic deformation of individual pebbles and the irreversible rearrangement of pebbles. Furthermore, other behaviour, like effective thermal conductivity and thermal expansion, depends sensitively on the packing and inter-particle force chains in the granular materials (Jaeger et al., 1996). To describe these properties, both a micro-mechanical description and a phenomenological model can be employed. The link between these micro- and macro-quantities can be studied by concurrent multiscale modelling. However, as sequential multiscale modelling, a micro-mechanics based phenomenological model for granular materials remains rare in literature.

Due to their discrete nature, in this paper, the constitutive behaviour of pebble beds will be studied by means of the discrete element method. The discrete element method (DEM), or distinct element method, was first introduced by Cundall and Strack (1979) to study the mechanical response of assemblies consisting of discrete particles. DEM has been employed in either dynamic or static analyses of granular media (Herrmann and Luding, 1998). DEM has been developed based on the idea that discrete particles could be displaced independently from one another and interact with each other only at contact points. Contact laws are applied to describe inter-particle forces, i.e., normal and friction forces. New contacts can be automatically detected. The interaction in the assembly is monitored contact by contact, and the motion of particles is modelled particle by particle. Using this method, the deformation, as well as the internal force distribution of the assembly can be obtained numerically (Thornton and Antony, 1998; Antony, 2000; Redanz and Fleck, 2001; Martin et al., 2003; Martin, 2004; Gilabert et al., 2007). These types of information are crucial to understand the mechanism of macroscopic behaviour of granular media, such as the yield surface (Redanz and Fleck, 2001) and the crush probability of single particles inside an assembly (Marketos and Bolton, 2007). Some early approaches have made some assumptions to simplify the problem under consideration, such as using two-dimensional cases, or simulating limited number of particles contained by rigid walls. However, these assumptions would not be valid if DEM is applied to pebble beds in fusion blankets.

With the help of DEM, thermal creep of a ceramic breeder pebble bed has been investigated by a 3D discrete numerical thermo-mechanics code (Lu et al., 2000; Ying et al., 2002). Recently, the contact force distribution inside pebble beds has been investigated (An et al., 2007a, b). For these existing studies, six rigid walls are applied as boundaries for the assembly containing a few thousand particles. Initial packing factors reached in these investigations are $60\pm0.5\%$. This range is below the reference value in fusion blanket applications. To provide a representative result, and to eliminate the effect of a rigid wall at the same time, a large number of particles should be considered. Periodic boundary conditions are hence essential to perform the discrete element simulation (Gilabert et al., 2007). Other researchers (Aquaro and Zaccari, 2005, 2006) simplify the particles in regular lattices as beam elements, which represent the interaction forces between pebbles, and the overall response can be obtained. By using regular lattices, analytical solutions can be obtained, and the initial packing factor can be varied by using different types of lattices. However, this approach eliminates the influence of the rearrangement of particles, which is another important factor to understand the overall plastic strains of the assembly.

Considering the micro-structure of pebble beds, the deformation mechanism can be clearly revealed by DEM approaches, including mechanical behaviour and thermal creep. The physical meanings of some phenomenological material parameters, such as strain-dependent thermal conductivity, can be explained through an investigation of assemblies consisting of particles. But on the other hand, the problem remains that, for example, the complexity of the micro-structure and the plastic contact of pebbles are still idealized in this approach. The homogenization of these microscopic informations should be studied in order to use results of DEM simulations in a different length scale. Moreover, engineering applications of DEM into large scale structures, such as a HCPB-TBM (helium cooled pebble beds-test blanket modulus) blanket, will not be practical without the help of continuum mechanics.

This paper is organized as follows. In Section 2, the theoretical background of the discrete element method will be briefly introduced, and a stress average method is presented to link the interactions between individual particles to the macroscopic stress state of the assembly. Some discussion concerning solution techniques will be made in Section 3. Finally, in Section 4, discrete element simulations to represent the uniaxial compression test of pebble beds are discussed.

2. Theory

2.1. Discrete element method

The discrete element method is applied to simulate an assembly of particles, in which it allows finite displacement and rotation of discrete bodies, including complete detachment (Thornton and Antony, 1998; Martin et al., 2003; Martin, 2004; Gilabert et al., 2007). A custom discrete element code has been developed for analysing pebble beds in this investigation. The kinematics of two contacting particles are schematically shown in Fig. 1. For normal interaction, only the elasticity of the bulk material is considered, and the particles are assumed to be spherically shaped. Thus, the classical Hertzian solution (Johnson, 1985) can be employed depending on the elastic properties of the contacting particles, i.e., I-th and J-th in the assembly, by

$$\mathbf{f}_N^{(I,J)} = -\tfrac{4}{3}E^*\sqrt{R^*}\delta^{3/2}\cdot\mathbf{n}. \tag{1}$$

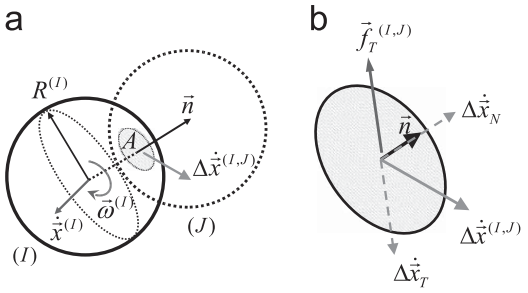

Fig. 1. (a) Kinematics of two contacting particles; (b) decomposition of the relative velocity in the contact region A.

Here, δ is the overlap of two contacting particles, $\mathbf{n}$ is the normal unit vector, E^* and R^* are the effective Young's modulus and the reduced radius, respectively, defined as

$$\frac{1}{E^*}=\frac{1-(\nu^{(I)})^2}{E^{(I)}}+\frac{1-(\nu^{(J)})^2}{E^{(J)}},\quad R^*=\frac{R^{(I)}R^{(J)}}{R^{(I)}+R^{(J)}}.$$

Ceramic breeder pebbles, such as Li_4SiO_4 considered in this investigation, are produced with good sphericity and with a narrow size range. For inelastic contact laws, there are different approaches in literature. Concerning the visco-plasticity properties of the bulk material, Storakers et al. (1999) have provided a solution using the total strain, which can be easily implemented in the present framework of the discrete element method. In order to take into account the elastic unloading path, Mesarovic and Johnson (2000) have investigated adhesive contact between elasto-plastic spheres, including the simplest case of the solution of perfect elasto-plastic contact. Kruggel-Emden et al. (2007) have reviewed the existing inter-particle contact laws used in discrete element methods. The friction force has a direction opposite to the sliding velocity $\Delta\dot{\mathbf{x}}_T$. The magnitude can be defined by different assumptions. For instance, the friction force applied to the I-th particle can be written as (Bicanic, 2004)

$$\mathbf{f}_T^{(I,J)}=-\frac{\Delta\dot{\mathbf{x}}_T}{|\Delta\dot{\mathbf{x}}_T|}\min(\mu f_N^{(I,J)},k_s|\Delta\dot{\mathbf{x}}_T|\cdot\Delta t). \tag{2}$$

Here, μ is the friction coefficient of the contacting surfaces, k_s represents the coefficient in the case of small tangential displacement (proportional to the sliding velocity), $f_N^{(I,J)}$ is the magnitude of the normal contact force between these two particles, and Δt is the time increment. The second part gives a smooth transition at the region of low relative tangential velocity $|\Delta\dot{\mathbf{x}}_T|$.

For the I-th particle, the time evolution of the degrees of freedom is governed by the equations

$$m^{(I)}\ddot{\mathbf{x}}^{(I)}=\sum_J\mathbf{F}^{(I,J)},\quad I^{(I)}\dot{\boldsymbol{\omega}}^{(I)}=\sum_J\boldsymbol{\Gamma}^{(I,J)}. \tag{3}$$

Here, $m^{(I)}$ and $I^{(I)}$ are the mass and the moment of inertia of particle I, respectively. $\mathbf{F}^{(I,J)}$ and $\boldsymbol{\Gamma}^{(I,J)}$ denote the inter-particle force and moment from the J-th particle on the I-th one. The most widely used method for integrating the equations of motion is the algorithm initially adopted by Verlet (1967). Swope et al. (1982) proposed a Verlet-equivalent algorithm, which stores positions, velocities and accelerations all at the same time t. Another important issue is the time step of each iteration for the explicit scheme. In this work, the time step is determined using the method proposed by Cundall and Strack (1979) as $\delta t=2f_t\sqrt{m_0/K_0}$, where f_t is less than unity to ensure stability of the calculation, m_0 is the smallest particle mass and K_0 is the maximum contact stiffness, defined by the contact law. Here, $f_t=0.4$, and thus a typical value of δt is around 10^{-7} s. The simulation for quasi-static deformation can be carried out either using a global damping method (Cundall and Strack, 1979) or by scaling the density of the particles by a factor of β with a typical value of $\beta=10^{12}$ (Thornton and Antony, 1998). The details will be discussed later in Section 3.

2.2. Micro–macro relations

The objective here is to determine the relation between the contact forces obtained in the discrete element calculation and the macroscopic stress tensor. This relation is necessary to link quantities from the length scales of a particle and the bed, and, thus, helps to understand the physics behind the macroscopic behaviour. In micro-mechanics, the unweighted volume average stress, taken over the volume V of the representative volume element (RVE), denoted by $\overline{\boldsymbol{\sigma}}$ is defined as

$$\overline{\boldsymbol{\sigma}}\equiv\frac{1}{V}\int_V\boldsymbol{\sigma}\,\mathrm{d}V. \tag{4}$$

Applying the Gauss divergence theorem and the equilibrium, $\sigma_{ij,i}=0$, of stresses, if both the body force and acceleration are zero, we have

$$\overline{\sigma}_{ij}\equiv\frac{1}{V}\int_V\sigma_{ij}\,\mathrm{d}V=\frac{1}{V}\oint_S\sigma_{lj}x_in_l\,\mathrm{d}S=\frac{1}{V}\oint_S\tilde{F}_jx_i\,\mathrm{d}S. \tag{5}$$

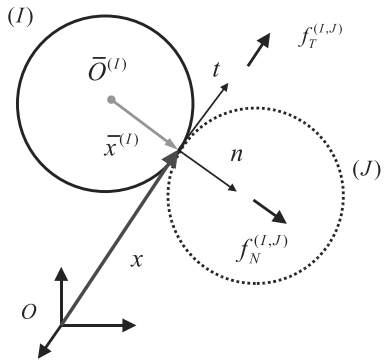

Fig. 2. Two contacting particles.

In this way, the macroscopic average stress $\overline{\sigma}_{ij}$ has been related to the external forces $\tilde{F}_j$ distributing on the surface S of the considered body.

A pair of contacting spherical particles, namely, the I-th and J-th particles, subject to discrete element analysis is illustrated in Fig. 2. To describe the coordinate of the contact point, it can be either denoted as $\overline{\mathbf{x}}^{(I)}$ in the local coordinate with respect to the origin $\overline{O}^{(I)}$ or as $\mathbf{x}$ in the global coordinate system with the origin O. In the following, these two approaches are discussed. All contacts are assumed to be point contacts, and thus for particle I,

$$\oint_S \tilde{F}_j x_i \,\mathrm{d}S = \sum_J F_j^{(I,J)} x_i^{(J)}. \tag{6}$$

Here, $x_i^{(J)}$ denotes the position of the contact point with particle J.

2.2.1. Local coordinates

It is convenient to place the origin $\overline{O}^{(I)}$ of the I-th particle coordinate system in the centre of the sphere, and the local coordinate system is named as $\overline{\mathbf{x}}^{(I)}$. In this pair of contacting particles, the relations

$$F_j^{(I,J)} = f_N^{(I,J)} n_j + f_T^{(I,J)} t_j,$$

$$F_j^{(I,J)} = -F_j^{(J,I)},$$

$$\overline{x}_i^{(I,J)} - \overline{x}_i^{(J,I)} = \delta^{(I,J)} n_i \tag{7}$$

are valid. Here, $f_N^{(I,J)}$ and $f_T^{(I,J)}$ are the magnitudes of the normal and tangential forces applied from particle J on I, $\delta^{(I,J)}$ denotes the distance between the centres of particles, and the unit vectors $\mathbf{n}$ and $\mathbf{t}$ are the normal and tangential unit vectors, respectively. The coordinate $\overline{x}_i^{(I,J)}$ describes the position of the J-th contact point in the local coordinate on particle I. The signs of the forces are defined by the vectors, i.e., a compressive force is negative. Since there is no stress present in the matrix (void), the integral of the assembly volume V can be obtained by summing each particle's volume $V^{(I)}(1 \le I \le N)$ in the assembly. Eq. (5) can be written for the N-particle assembly by summing up all the existing contact pairs

$$\int_V \sigma_{ij} \,\mathrm{d}V = \sum_{I=1}^{N} \int_{V^{(I)}} \sigma_{ij} \,\mathrm{d}V = \sum_{I=1}^{N} \oint_{S^{(I)}} \tilde{F}_j \overline{x}_i^{(I)} \,\mathrm{d}S = \sum_{I=1}^{N} \sum_J F_j^{(I,J)} \overline{x}_i^{(I,J)}. \tag{8}$$

With Eqs. (7) and (8), the average stress can be obtained as

$$\overline{\boldsymbol{\sigma}} = \frac{1}{V} \left(\sum_{I<J} \delta^{(I,J)} f_N^{(I,J)} \mathbf{n} \otimes \mathbf{n} + \sum_{I<J} \delta^{(I,J)} f_T^{(I,J)} \mathbf{n} \otimes \mathbf{t} \right). \tag{9}$$

This equation is consistent with the derivation by Christoffersen et al. (1981), and it has been implemented in DEM calculation in literature (Thornton and Antony, 1998; Martin et al., 2003; Martin, 2004; Gilabert et al., 2007).

2.2.2. Global coordinates

For the global coordinate system, a simulation box has been sketched in Fig. 3. The contact forces in Eq. (5), of two contacting particles inside the simulation box, are opposite while the position $\mathbf{x}$ is identical. Therefore, the summation over all interactions between particles inside the simulation box is zero. Only the terms stemming from contacts across the

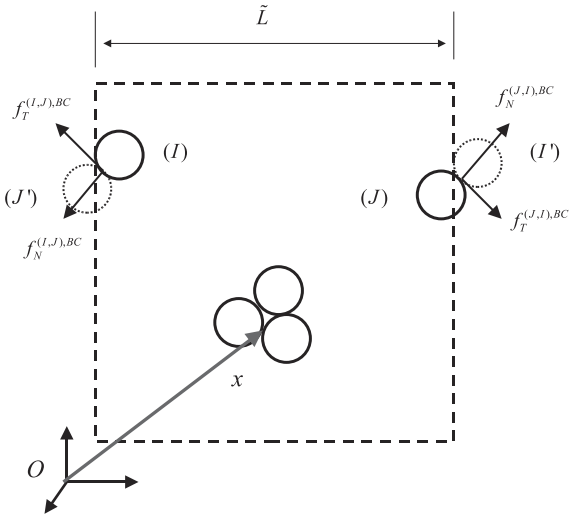

Fig. 3. Average stress using the global coordinate.

boundaries are non-zero. Considering two types of boundary conditions, we have:

- Generalized boundary conditions

$$\overline{\sigma}_{ij} = \frac{1}{V}\sum_{I}\sum_{BC} F_j^{(I,BC)} x_i. \tag{10}$$

- Periodic boundary conditions

$$\overline{\sigma}_{ij} = \frac{1}{V}\sum_{I<J} F_j^{(I,J),BC} \tilde{L}_i^{(J)}. \tag{11}$$

In the first case, the interaction $\mathbf{F}^{(I,BC)}$ denotes the interactions between the I-th particle and objects outside the box (e.g., the wall condition). In the second case of periodic boundary conditions, two contacts exist on the corresponding boundaries of the box, as shown in Fig. 3. The J-th particle has been shifted by the vector $\tilde{\mathbf{L}}^{(J)}$, in order to satisfy the periodic boundary conditions, and as a result, it contacts with I-th particle inside the box. By summing up the corresponding interactions, the second expression can be obtained.

2.2.3. Discussion on the averaging methods

Being independent of observers, the stress tensors obtained from both coordinates systems have to be identical. This can be proven from the DEM calculation, by implementing both methods and comparing to each other. There are some differences between these two methods:

- The first method, using the local coordinate, can be employed to calculate the local stresses inside the simulation box, for instance, the stress state of a small assembly of particles.
- The latter method, using global coordinates, can be also applied for systems of non-spherical particles. In this case, the first method is no longer valid, since Eq. (7) is not fulfilled.
- The latter method is more cost-efficient for larger system, since only the summation over particles on the boundaries is taken into consideration. However, the difference is ignorable in the calculation of systems of a limited number of particles.
- Both methods are obtained for the assumption of zero body force, as well as the term of the acceleration $\rho\ddot{\mathbf{x}}$. Therefore, during the DEM calculation, an additional criterion has to be adopted to ensure a quasi-static state, and to obtain the exact macro-stresses from the current assembly. The real quasi-static state has not been reached until the difference

$$\left|\frac{\sigma_{ii}^{(\mathrm{ext})} - \sigma_{ii}^{(\mathrm{int})}}{\sigma_{ii}^{(\mathrm{int})}}\right| < \varsigma$$

  is smaller than a certain value. Here, the subscripts (ext) and (int) indicate the global and local methods, respectively, and ς is a tolerance.
- If only normal contact is considered, Eq. (9) ensures the symmetry of the stress tensor. On the contrary, Eq. (11) would provide a slightly asymmetric tensor during the calculation.

- Moreover, in strain-controlled tri-axial compression, the shear stresses are not exactly zero, but a few magnitudes smaller than the normal stresses. This is caused by a slightly anisotropic packing state, which will be ignorable by using systems of a larger number of particles.

3. Solution techniques

In this section, some techniques used in the current discrete element study will be discussed. Periodic boundary conditions (PBCs) for the simulation box, as well as strain- and stress-controlled mechanical loading, has been implemented. The convergence condition and the damping methods to accelerate the convergence rate are also discussed.

3.1. Periodic boundary conditions

Since the main focus in this investigation is to study the bulk behaviour of this type of materials, periodic boundary conditions have to be considered. The initial periodic configuration is formed by shifting the particles in the objective zone, a representative volume element (RVE), by a vector $\mathbf{L}^{(n)}$ to the (n)-th periodic zone, where $n=1,\ldots,26$ in the three dimensional case. After an infinitesimal deformation, the RVE has an overall strain tensor $\boldsymbol{\varepsilon}$, and the change of $\mathbf{L}^{(n)}$ can be represented by the strain tensor. Here, the vector $\mathbf{L}^{(n)}$ changes to vector $\tilde{\mathbf{L}}^{(n)}$ with respect to the strain tensor $\boldsymbol{\varepsilon}$ as

$$\tilde{\mathbf{L}}^{(n)} = (\mathbf{I}+\boldsymbol{\varepsilon})^{\mathrm{T}} \cdot \mathbf{L}^{(n)}. \tag{12}$$

Here, $\mathbf{I}$ is the second order identity matrix and δ_{ij} is the Kronecker delta. Fig. 4 shows the vector $\tilde{\mathbf{L}}^{(n)}$ varies with respect to the strain tensor $\boldsymbol{\varepsilon}$.

3.2. Ways of mechanical loading

Changing the strain tensor, strain control of the RVE can be realized by Eq. (12). In order to control the deformation of the periodic cell, an incremental strain tensor $\Delta\varepsilon_{ij}$ is specified, according to which the centres of all the particles in the assembly are initially moved by $\Delta x_j = \Delta\varepsilon_{ij}x_i$, at the beginning of each loading step, as if they are points in a continuum. Then the calculations to reach the equilibrium state are carried out iteratively. The applied deformations of particles in the RVE result in stresses, which can be calculated by interaction forces, see Eq. (9) or (11).

Moreover, to implement stress proportional loading, the stress can be controlled by a proportional–integral–derivative (PID) controller (Ziegler and Nichols, 1993). The PID controller algorithm involves three separate parameters: the proportional, integral and derivative values. The proportional value determines the reaction to the current error $e(t)$, the integral value determines the reaction based on the sum of the recent errors and the derivative one determines the reaction to the rate at which the error has been changing. The weighted sum of these three actions is used to adjust the process via a control element. The manipulated variable (MV) can be expressed as the standard form of the PID controller in devices as

$$\mathrm{MV}(t) = K_p\left[e(t)+\frac{1}{T_i}\int_0^t e(\tau)\,\mathrm{d}\tau + T_d\frac{\mathrm{d}e(t)}{\mathrm{d}t}\right], \tag{13}$$

where K_p is the proportional gain, and T_i and T_d are the integral time and derivative time, respectively.

Assuming the materials being initially isotropic, the incremental form of Hook's law can be expressed in the Cartesian coordinate system (x_1,x_2,x_3) as

$$\mathrm{d}\varepsilon_{ij} = \frac{1}{E^*}[(1+\nu)\,\mathrm{d}\sigma_{ij} - \nu\delta_{ij}\,\mathrm{d}\sigma_{kk}]. \tag{14}$$

If $\overline{\sigma}_{ij}^{(n)}$ is the desired value of stress and $\sigma_{ij}^{(n)}$ is the calculated value, the strain tensor can be updated by the current error $\mathrm{d}\sigma_{ij}^{(n)} = \overline{\sigma}_{ij}^{(n)} - \sigma_{ij}^{(n)}$ of the stress tensor and the counterpart $\mathrm{d}\sigma_{ij}^{(n-1)}$ at the previous step, in the framework of the PID

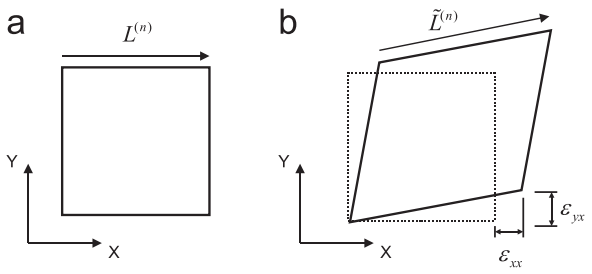

Fig. 4. A schematic drawing of the vector $\tilde{\mathbf{L}}^{(n)}$: (a) the initial configuration and (b) an infinitesimally deformed shape.

controller as

$$\mathrm{d}\varepsilon_{ij}^{(n)} = \mathrm{d}\varepsilon_{ij}^{P,(n)} + \mathrm{d}\varepsilon_{ij}^{I,(n)} + \mathrm{d}\varepsilon_{ij}^{D,(n)},$$

$$\varepsilon_{ij}^{(n)} = \varepsilon_{ij}^{(n-1)} + \mathrm{d}\varepsilon_{ij}^{(n)}. \tag{15}$$

Here, the respective contributions of the PID parts are

$$\mathbf{P}: \quad \mathrm{d}\varepsilon_{ij}^{P,(n)} = \frac{1}{E^*}[(1+\nu)\,\mathrm{d}\sigma_{ij}^{(n)} - \nu\,\mathrm{d}\sigma_{kk}^{(n)}\delta_{ij}],$$

$$\mathbf{I}: \quad \mathrm{d}\varepsilon_{ij}^{I,(n)} = \mathrm{d}\varepsilon_{ij}^{I,(n-1)} + \frac{1}{E^*}\frac{\mathrm{d}t}{T_i}[(1+\nu)\,\mathrm{d}\sigma_{ij}^{(n)} - \nu\,\mathrm{d}\sigma_{kk}^{(n)}\delta_{ij}],$$

$$\mathbf{D}: \quad \mathrm{d}\varepsilon_{ij}^{D,(n)} = \frac{1}{E^*}\frac{T_d}{\mathrm{d}t}[(1+\nu)(\mathrm{d}\sigma_{ij}^{(n)} - \mathrm{d}\sigma_{ij}^{(n-1)}) - \nu(\mathrm{d}\sigma_{kk}^{(n)} - \mathrm{d}\sigma_{kk}^{(n-1)})\delta_{ij}]. \tag{16}$$

Therefore, by summing up these parts, we have

$$\mathrm{d}\varepsilon_{ij}^{(n)} = \mathrm{d}\varepsilon_{ij}^{I,(n-1)} + \frac{1+\nu}{E^*}\left[\left(1+\frac{\mathrm{d}t}{T_i}\right)\mathrm{d}\sigma_{ij}^{(n)} + \frac{T_d}{\mathrm{d}t}(\mathrm{d}\sigma_{ij}^{(n)} - \mathrm{d}\sigma_{ij}^{(n-1)})\right] - \frac{\nu}{E^*}\delta_{ij}\left[\left(1+\frac{\mathrm{d}t}{T_i}\right)\mathrm{d}\sigma_{kk}^{(n)} + \frac{T_d}{\mathrm{d}t}(\mathrm{d}\sigma_{kk}^{(n)} - \mathrm{d}\sigma_{kk}^{(n-1)})\right]. \tag{17}$$

The value of E^* and ν can be set rather arbitrarily, and they are not necessarily equal to the ones of the assembly. If we only consider the integral part of the PID controller, as $\mathrm{d}\varepsilon_{ij}^{(n)} = \mathrm{d}\varepsilon_{ij}^{I,(n)}$, and set $\nu = 0$, we have the form of

$$\dot{\varepsilon}_{ij}^{(n)} = \dot{\varepsilon}_{ij}^{(n-1)} + \frac{1}{E^* T_i}\mathrm{d}\sigma_{ij}^{(n)}. \tag{18}$$

Thus, the general form in Eq. (17) implicitly contains the servo-control of strain rate used in literature (Thornton and Antony, 1998; Antony, 2000) as a special case.

Since the particle assembly has a random structure (slight anisotropy), a small shear strain/stress is present, if the principle stresses/strains are applied on the assembly. Two strategies can be used to eliminate either shear stresses or shear strains: (1) let $\varepsilon_{ij} = 0$ for $i \neq j$, and accept shear stresses to be present; or (2) let $\sigma_{ij} = 0$ for $i \neq j$, and accept shear strains to be present.

3.3. Convergence control

The most simple example for the determination whether a system reaches the equilibrium state is a single spring–mass system. In terms of energy, all systems have two types of energy, potential energy $\mathcal{V}$, and kinetic energy $\mathcal{K}$. When a spring is stretched or compressed, it stores elastic potential energy, which may then transfer into kinetic energy. If the system is a dissipative one (e.g., a spring-dashpot-mass system), the total energy will finally be transformed into heat. The steady-state can be reached eventually (as $t \to \infty$) by not only minimizing potential energy ($\min \mathcal{V}$) but also removing all kinetic energy ($\mathcal{K} = 0$).

In an assembly, the network of contacts can also be simplified into spring-dashpot-mass systems. Thus, to achieve convergence in such a simple system, the criterion of unbalanced force is not sufficient for equilibrium. Additionally, the criterion of the kinetic energy should be taken into account. The principle stays unchanged for the whole assembly. The velocity (kinetic energy) and acceleration, representing the unbalanced force, of particles should be checked at the same time. The criteria can be expressed as

$$\delta f \leq \delta f_0, \quad \overline{\mathcal{K}} \leq \mathcal{K}_0. \tag{19}$$

Here, δf_0 and K_0 are two inputs for the convergence criteria, namely maximum allowable unbalanced force and maximum allowable average kinetic energy, respectively.

For force convergence (unit: N), we have

$$\delta f_0 \leq \max(\delta f_{\min}, \alpha_0 \cdot f_{\mathrm{ave}}), \tag{20}$$

where f_{ave} is the average contact force in the assembly, and the tolerance for the unbalanced force $\delta f_{\min}$ and the ratio to the average contact force α_0 are constants. The average kinematic energy (unit: J) of the assembly is given by

$$\overline{\mathcal{K}} = \frac{1}{N}\sum_{I=1}^{N}\left[\frac{1}{2}m^{(I)}(\mathbf{v}^{(I)})^2 + \frac{1}{2}I^{(I)}(\boldsymbol{\omega}^{(I)})^2\right]. \tag{21}$$

In this investigation, we assume that the equilibrium state of the assembly is not reached, until Eq. (19) is satisfied.

3.4. Damping method

In order to remove the kinetic energy and to achieve convergence inside the assembly, a dissipation mechanism should be introduced. This is divided into two parts: local damping and global damping.

For the I-th and J-th particles in contact, if only the dependence on the relative normal velocity $\dot{\mathbf{x}}_N^{(I,J)}$ is taken into account, the local damping force is given by

$$\mathbf{f}_d^{(I)} = -m_{\text{eff}}\eta_d\dot{\mathbf{x}}_N^{(I,J)}. \tag{22}$$

Here, $m_{\text{eff}} = m^{(I)}m^{(J)}/(m^{(I)}+m^{(J)})$ is the reduced mass. The local damping factor η_d can be found for different materials in Kruggel-Emden et al. (2007). The local damping forces will vanish when relative velocities $\dot{\mathbf{x}}_N^{(I,J)}$ are approaching zero.

In addition to local damping, a global damping mechanism is introduced to speed up convergence. For the I-th particle, the global damping force is

$$\mathbf{f}_D^{(I)} = -m^{(I)}\eta_D\dot{\mathbf{x}}^{(I)},$$

$$\mathbf{\Gamma}_D^{(I)} = -I^{(I)}\eta_D\boldsymbol{\omega}^{(I)}. \tag{23}$$

Here, η_D is the global damping factor. Similar to the local damping mechanism, global damping forces will vanish when velocities $\dot{\mathbf{x}}^{(I)}$ and $\boldsymbol{\omega}^{(I)}$ are approaching zero. For a quasi-static analysis, global damping can be used to absorb the kinetic energy, and enhance the convergence rate to the equilibrium for the assembly.

4. Simulation of uniaxial compression tests

In this section, simulations of uniaxial compression tests on assemblies of Li_4SiO_4 pebbles are carried out using the discrete element method. This type of experiments has been used to characterize the thermo-mechanical behaviour of pebble beds (Reimann et al., 2002, 2005). In this work, we consider "soft" compaction, meaning, compaction without sintering and crushing.

The loading conditions of the assembly are defined by the macro-strain tensor: ε_{33} increases from 0 to 1.25% and the other components are zero. Periodic boundary conditions for the assembly are implemented by Eq. (12) with respect to the current configuration, and the overall stress tensor is calculated by Eq. (9).

4.1. Material parameters

Young's modulus for bulk Li_4SiO_4 has been measured by Dienst and Zimmermann (1988) and Zimmermann (1989), and it depends on both porosity of the material and temperature. The relation is expressed as

$$E = 110(1-\tilde{p})^3 \times [1 - 2.5\times10^{-4}(T-293)]\ (\text{GPa}). \tag{24}$$

Here, $\tilde{p}$ is the porosity of the bulk material and T is the temperature in Kelvin. For Li_4SiO_4 pebbles, $\tilde{p} = 5-6\%$ (Knitter et al., 2007), and the temperature is around 20 °C. Therefore, the material parameters are set as $E = 90$ GPa and $\nu = 0.24$. Only elastic contact is taken into account in this simulation, which seems to be justified, since the bulk material is Li_4SiO_4 ceramic in this study, whose plastic deformation is negligible. The normal interaction is described as Eq. (1), and the elastic potential energy for each contact is $\frac{8}{15}E^*\sqrt{R^*}\delta^{5/2}$. The density of the bulk material is 2260 kg/m^3 (Loebbecke and Knitter, 2007). For tangential interactions, the friction coefficient is set to 0.1 due to lack of experimental data. A low friction coefficient increases instability of the assembly and introduces larger displacements of particles. As a result, it reduces overall loads (Procopio and Zavaliangos, 2005).

The parameters for the convergence control introduced in Section 3 can be found in Table 1, namely the tolerance for unbalanced force $\delta f_{\min}$ and the ratio to the average contact force α_0, the maximum allowable average kinetic energy $\mathcal{K}_0$, the local damping factor η_d, and the global damping factor η_D. The tolerance $\delta f_{\min} = 5\times10^{-4}$ N will introduce an error of a few kPa to the stress tensor, while the damping factors result in dissipation forces with a magnitude of less than 1×10^{-4} N after convergence is reached. Experience in calculations shows that these settings are quite strict, and thus errors should be negligible.

Mono-sized pebbles are generated in the range of packing factors from 63.3% to 64.4% with the random close packing algorithm proposed by Jodrey and Tory (1985), and the diameter of pebbles is set to 0.5 mm. This algorithm provides the possibility to control the initial packing factor without introducing any initial stress state (Gan et al., 2009). The samples are divided into three groups of packing factors: (Low) 63.3–63.5%, (Medium) 63.7–63.9% and (High) 64.0–64.4%, as listed in Table 2. The number of particles in this simulation is 5000. Since periodic boundary conditions are applied, the number of particles seems to be sufficient to give a representative result (Gusev, 1997, 2007).

Table 1
Parameters for the convergence control.

$\delta f_{\min}$ (N)	α_0 (1)	$\mathcal{K}_0$ (J)	η_d (1/s)	η_D (1/s)
5×10^{-4}	5×10^{-4}	1×10^{-12}	5×10^{4}	5×10^{4}

Table 2
Packing factors of the samples.

Number	L: 63.3–63.5%	M: 63.7–63.9%	H: 64.0–64.4%
1	0.63393841	0.63728178	0.64007780
2	0.63411831	0.63772953	0.64166147
3	0.63479272	0.63859036	0.64355432

4.2. Stress–strain curves

The macro-strain $\varepsilon_{33} = -1.25\%$ is applied incrementally to the assemblies, and the stress σ_{33} is calculated from the interaction forces. After loading, the assemblies are unloaded by gradually removing ε_{33} until the stress σ_{33} reaches zero. Fig. 5 shows the stress–strain curves from discrete element simulations of assemblies with (a) low, (b) medium and (c) high initial packing factors, and a typical experimental curve (Reimann et al., 2005) is plotted as the dashed line for comparison.

The loose-packed assemblies deform significantly up to $\varepsilon_{33} = -0.4\%$ for small compressive stresses. Then stresses are gradually built up, see Fig. 5(a). This suggests that for a loose-packed assembly applying small compressive stresses (i.e., a few kPa) can increase the packing factor without introducing notable residual stresses inside the assembly. The response of those assemblies is more compliant than the experimental curve. The congruent unloading paths of simulations and the experimental curve can be found, although shifts about $\Delta\varepsilon_{33} = 0.5\%$ are present in those assemblies. This indicates that the elastic constants, e.g., Young's modulus, of the assembly depend on the stress state rather than on compressive strains. Friction forces (Makse et al., 2000) and rolling resistance (Gilabert et al., 2007) can form a jammed system and hence lead to a build-up of stresses inside the assembly (Goldenberg and Goldhirsch, 2005; Richard et al., 2005). However, in this study the friction coefficient is set to a comparably low value of 0.1 and no rolling resistance has been taken into account with the goal of making a first step towards the discrete element simulation of pebble beds. Assemblies with medium packing factors agree satisfactorily with the experimental curve, see Fig. 5(b). The maximum compressive stresses reached at end of loading are comparable to the experiment. The unloading path shows a similar trend parallel to the experiment, and, furthermore, gives a macroscopic irreversible strain at the end of unloading, which can be compared quantitatively to the experimental curve. The close-packed assemblies, in Fig. 5(c), show a much stiffer response than the experiment. Relatively small irreversible strains can be found. Such assemblies can represent the behaviour of densified pebble beds after a few cyclic compressive loadings. For the extreme case of $\eta = 64.36\%$, the compressive stress reaches almost 8 MPa at the end of loading. The simulation shows that the initial packing factor plays an important role in the mechanical response, and the group with medium packing factor gives the best fit to the experimental data. The packing factor in the experiments is 63.5% for the dashed line shown in Fig. 5 (Reimann et al., 2005). The experimental stress–strain curve was extracted from a cylindrical container with dimensions much larger than the size of pebbles, thus, the experiments are governed by bulk behaviour of pebble beds and the contribution of the near wall regions is small. The overall packing factor in the experiments consists of both bulk and near wall regions, and it approaches to the one in the bulk region considering the dimensions of the container. However, the wall region usually has a lower packing factor (Reimann et al., 2008; Gan et al., 2009). The packing factor in the bulk region will be slightly higher than the average value, 63.5%. Therefore, the experiment has to be compared to the group of simulations with medium packing factors (M1, M2, M3) in Fig. 5(b). It can clearly be seen that this comparison shows qualitatively and quantitatively good agreement.

In summary, the stress–strain curves of three groups differ significantly, suggesting that the sensitivity to the packing factor is an important issue in pebble beds related problems. Overall plastic strains are observed for the assemblies, despite the fact that only elastic interactions are taken into account in this investigation. The macroscopic irreversibility found in the present discrete element simulations has to be attributed to rearrangement of elastic particles.

4.3. Visualization of the assembly

With the help of OpenGL®, a visualization software has been developed to visualize outputs from the discrete element simulation. Fig. 6 shows the force chains and the elastic potential energy of an assembly at different loading levels. Two loading steps of the assembly M1 are chosen as shown in Fig. 5(b). The magnitudes of the strain ε_{33} are 0.75% and 1.25%. The unit of normal contact forces is N, and the unit of elastic potential energy is 10^{-6} J. The potential energy depends on both magnitude and number of contact forces. Close examination of the positions showed rearrangements of particles at different loading levels.

Force chains are formed at the low strain level, and evolve during loading. Main force chains are developing during loading and support the whole assembly. Non-uniform distributions of both potential energy and inter-particle forces are observed. The force chains are important for the understanding of the mechanism of heat transfer inside the assembly, especially for those materials with high ratio of solid-to-gas thermal conductivities, such as beryllium pebbles. The main

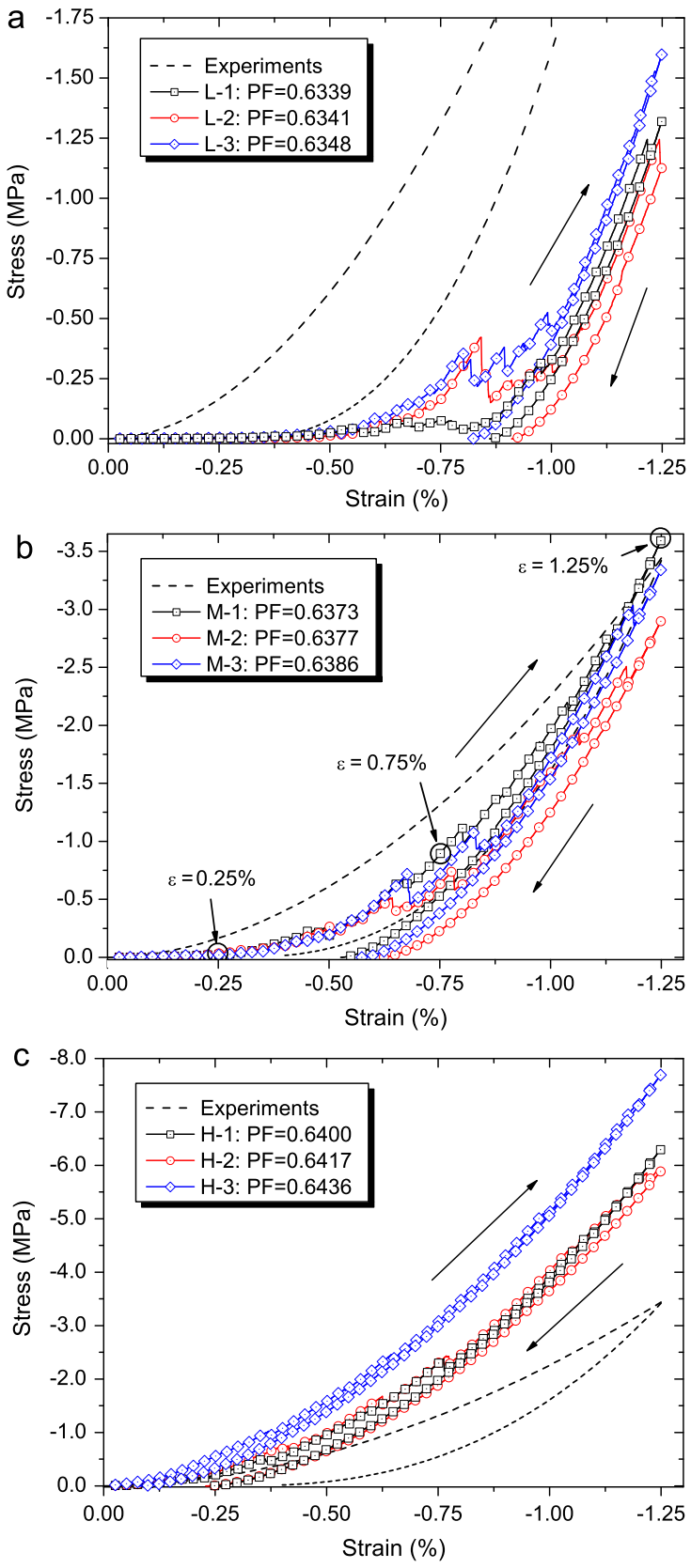

Fig. 5. Stress–strain curves of discrete element simulations of uniaxial compression tests, assemblies with: (a) low; (b) medium; (c) high packing factors.

force chains, carrying most of the external load, have less thermal resistance to the heat flux transferring through the assembly. Based on discrete element methods, it will be possible to formulate an anisotropic thermal conductivity taking into account the loading history.

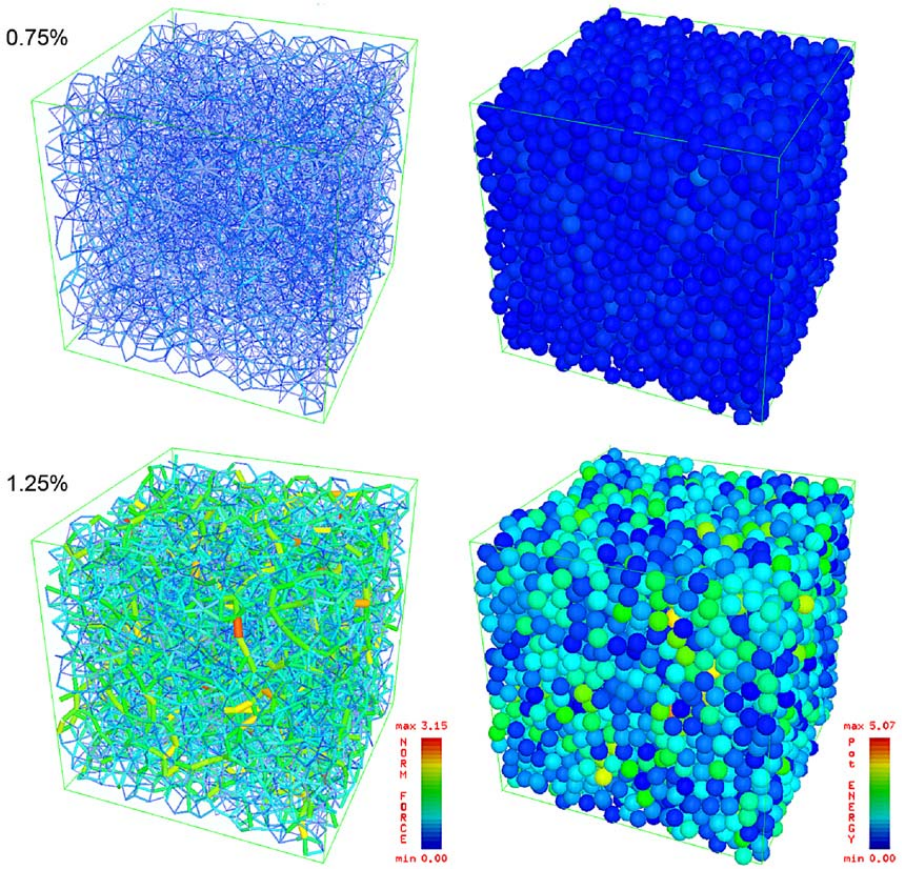

Fig. 6. Visualization of simulation results: left, inter-particle force chains (unit: N); right, elastic potential energy (unit: $10^{-6}J$).

4.4. Statistical analyses

In addition to the macroscopic quantities, such as stresses and strains, the interactions can be obtained explicitly by the discrete element simulation. We focus on the probability distribution of normal contact forces, as well as mean values of coordination number and contact forces in dependence on the macroscopic stress state. Here, the coordination number is the total number of contacting neighbours of a central particle.

Fig. 7 shows probability density distributions of the normalized normal forces $f^{(I,J)}/f_{\mathrm{ave}}$ and normalized maximum normal forces $f^{(I)}_{\mathrm{max}}/f_{\mathrm{ave}}$ in two assemblies, namely M1 and H3. The average normal force f_{ave} is the mean value of all normal interactions inside the assembly, and the maximum normal force $f^{(I)}_{\mathrm{max}}$ of each particle is defined as the maximum absolute value among all the normal forces applied on this particle.

For both types of probability density distributions, similarities are found not only in different loading levels, namely 0.25%, 0.75%, 1.00% and 1.25%, but also between the two chosen assemblies. Despite the fact that at different loading levels the average normal contact force and the coordination number (C.N.) in the same assembly vary in a wide range, nearly congruent probability density distributions can be found. Fig. 7(a) and (c) show non-uniform distributions of the normalized normal forces. A small fraction of the normal forces is in the high $f^{(I,J)}/f_{\mathrm{ave}}$ ratio region. The peak of the distribution is located in the region $f^{(I,J)}/f_{\mathrm{ave}} < 1.0$. In Fig. 7(b) and (d), however, the peak of the probability distribution of the normalized maximum contact force is located at $f^{(I,J)}/f_{\mathrm{ave}} \approx 1.5$, suggesting that most of the particles inside the assembly have a maximum contact force larger than f_{ave}. Moreover, we introduce fit functions for the two types of normalized contact forces. We assume that the cumulative distribution functions of both types have the form of the Weibull distribution

$$P(x) = 1 - \exp\left[-\left(\frac{x}{k}\right)^m\right], \tag{25}$$

where x is the normalized contact force, m and k are the shape parameter and scale parameter of the distribution, respectively. The maximum likelihood method was employed to find these Weibull parameters from the force distributions of different samples. Table 3 shows the parameters obtained from the simulation data. The mean values of all samples and standard deviations (SD) are also shown in the table. As a result, it turns out that the mean values of these two types of force distributions represent well the force chains developed during loading in all assemblies with different initial packing factors.

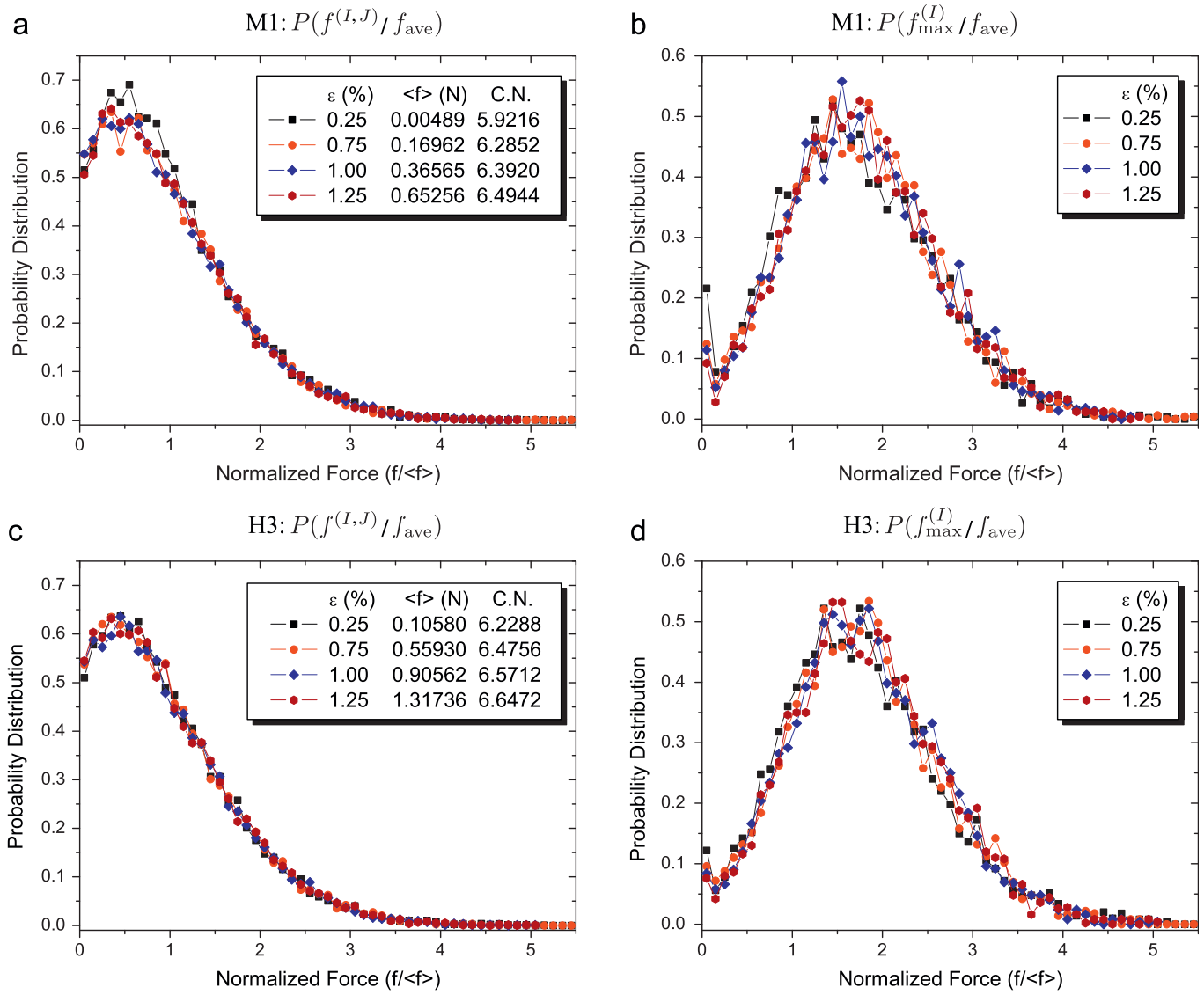

Fig. 7. Probability density distributions of: (a), (c) the normalized normal contact forces and (b), (d) normalized maximum normal contact forces of M1 and H3, respectively.

Table 3
Parameters for the Weibull distribution of normalized contact forces.

x	$f^{(I,J)}/f_{ave}$		$f^{(I)}_{max}/f_{ave}$	
Sample	m	k	m	k
L1	1.39481	1.10734	2.41910	1.98127
L2	1.34912	1.10201	2.30538	2.00193
L3	1.35363	1.10128	2.32980	2.00033
M1	1.36191	1.10357	2.37626	2.02316
M2	1.35353	1.10384	2.38968	2.02029
M3	1.37461	1.10704	2.45238	2.01730
H1	1.40230	1.11023	2.53839	2.02390
H2	1.36118	1.10059	2.40291	2.03724
H3	1.33579	1.10166	2.42987	2.05977
Mean	1.36521	1.10417	2.40486	2.01835
SD	0.02169	0.00331	0.06846	0.02264

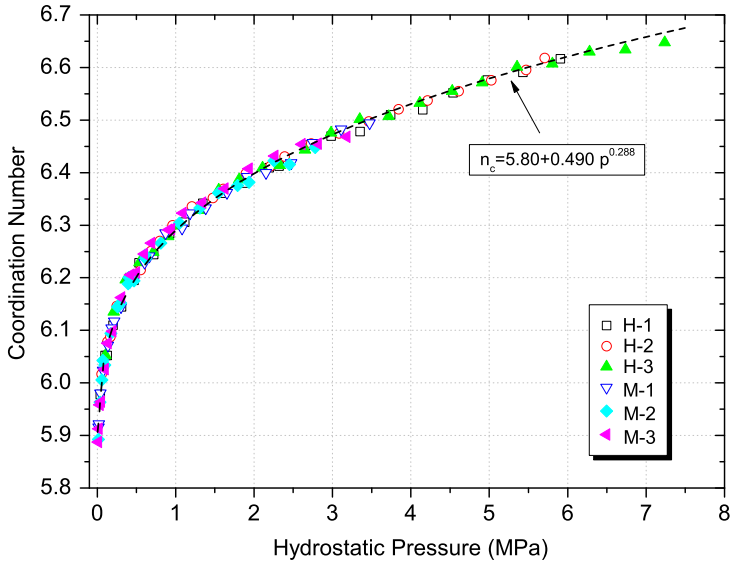

Fig. 8. Average coordination number over macroscopic hydrostatic pressure.

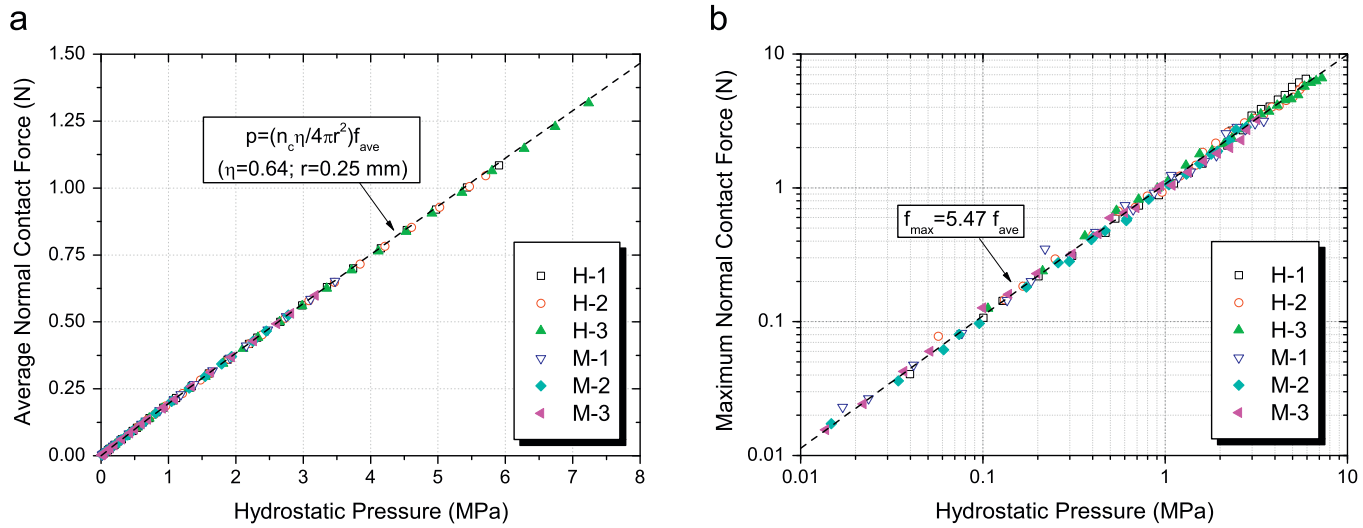

Fig. 9. Contact forces over hydrostatic pressure: (a) average normal forces; and (b) maximum normal forces.

The change of the average coordination number, named as n_C, of an assembly over the macroscopic hydrostatic pressure, $p = -\sigma_{ii}/3$, is plotted in Fig. 8. Assemblies with medium and high packing factors are represented, and the ones with low packing factors are excluded from the figure since their macroscopic stresses only vary in relatively small ranges. The average coordination number varies between 5.8 and 6.7, for hydrostatic pressures from 0 to 8 MPa. It rapidly increases with the increase of compressive stresses in the low stress region, suggesting rearrangement of particles during loading. New contacts are formed as a result of the compressive stress state, which in turn increases the stiffness of the assembly. Eventually the average coordination number becomes less sensitive to the increase of hydrostatic pressure, suggesting a saturation value of n_C. The distribution of the data points gives the possibility to fit those data with a simple function. Equation

$$n_C = 5.80 + 0.490 p^{0.288} \tag{26}$$

gives the best fit for data of different cases between 0 and 8 MPa. This fit curve is also plotted in Fig. 8 as a dashed line for comparison. The average coordination number is an important quantity. It plays, for instance, an important role for the strain-dependent effective thermal conductivity of pebble beds (Reimann et al., 2008), which is also one of the critical issues in design and analysis of blanket systems. Therefore, it is essential to know the dependence of the average coordination number on the load.

Fig. 9 shows the changes of contact forces, namely the average normal contact forces f_{ave} and the maximum contact forces f_{max} in assemblies with medium and high packing factors, over the hydrostatic pressure. Here, the average normal

contact force is

$$f_{\text{ave}} = -2\sum_{I<J} f_N^{(I,J)}/(n_C \cdot N). \tag{27}$$

For the calculation of the hydrostatic pressure, $p = -\sigma_{ii}/3$, from Eq. (9), $n_i n_i = 1$ and $n_i t_i = 0$. Neglecting the changes of the distance between two contacting particles, we have

$$p = -\frac{2r}{3V}\sum_{I<J} f_N^{(I,J)}. \tag{28}$$

For mono-sized assemblies, the initial packing factor can be written as $\eta = N \cdot \frac{4}{3}\pi r^3/V$, where r is the particle radius. Thus, the hydrostatic compression can be expressed as follows:

$$p = \frac{n_C \eta}{4\pi r^2} f_{\text{ave}}. \tag{29}$$

Here, the initial packing factor is chosen as $\eta = 0.64$ for all samples and the average coordination number n_C is calculated by Eq. (26). Nemat-Nasser (2000) provided a similar relation for 2D cases, but here the dependency on not only the average normal contact force but also the coordination number is shown. The present expression takes into account the contribution of the rearrangement of particles inside the assembly, i.e., the dependence of n_C on the load. In Fig. 9(a), the approximation curve is plotted and gives a good representation of the data. Due to the occurrence of the radius, this relation can also be applied to different systems with other values of particle radius.

Fig. 9(b) shows the maximum forces $f_{\max}$ inside the assemblies, with respect to hydrostatic pressure. Usually, the maximum force is 5–6 times of the average normal force in an assembly. Neglecting scatter in the data of the maximum force, the relation

$$f_{\max} = (5.47 \pm 0.474) f_{\text{ave}} \tag{30}$$

gives the best linear fit for the maximum force as a function of the average force. This curve is plotted in Fig. 9(b), agreeing well with the data from simulations. The maximum force $f_{\max}$ is important for the crush probability of individual pebbles. Eqs. (29) and (30) make it possible to estimate the maximum contact force based on the value of hydrostatic pressure.

For the crushing of single pebbles in a pebble bed, the following factors are essential: the contact force distributions $P(f)$ and $P(f_{\max})$, the coordination number n_C, the maximum contact force $f_{\max}$ in the assembly, as well as the behaviour of single pebbles (Marketos and Bolton, 2007). Except for the last factor, which needs systematical experimental study on the crush load of single pebbles, the discrete element simulations presented here are capable to describe all those issues mentioned above. This offers possibility to investigate the complex blanket system by means of simple experiments.

DEM simulations for common granular materials usually include many simplifications, concerning, for instance, size-distribution and shape of particles under consideration. In literature, there are many available DEM tools, including commercial software. However, there are only a few comparisons between simulation and experiment, since in experiments it is difficult to have an appropriate size ratio of pebble diameter and container dimensions, as well as to have available particles of close to ideal shape. In the current case, the uniaxial compression test was carried out in large containers to achieve bulk properties, and the granular material has been produced under controlled conditions with (1) good sphericity and (2) narrow diameter range. DEM simulations of such simple systems, where common simplifications are justified in a natural manner, and the comparison to corresponding experimental data show not only that DEM is a promising tool in future applications, but also supports and justifies the DEM theory proposed in recent decades as a valuable numerical tool.

5. Conclusion

In this paper, the discrete element method has been used to analyse the mechanical response of assemblies of pebbles. In addition to the basic theoretical background of DEM, the micro–macro relations have been investigated to relate inter-particle contacts to the macroscopic stresses. The simulation of uniaxial compression tests of Li_4SiO_4 pebble beds shows that the initial packing factor plays an important role in the mechanical response to the external excitation. Three groups of assemblies with a given initial packing factor (with low, medium and high packing factors, respectively) have been prepared and studied. The group with medium packing factor, which is the packing factor closest to the experiments, can be quantitatively compared to experimental data in terms of overall stress–strain curve. A macroscopic irreversible deformation of pebble beds has been observed for assemblies with only elastic particles, suggesting that the rearrangement of particles is an important mechanism for macroscopic irreversibility. For different external loading levels and samples, the normalized force distributions are the same in view of statistics. Furthermore, the average coordination number, as well as the average and maximum normal contact forces are obtained as a function of the macroscopic hydrostatic pressure. This investigation gives not only a basic understanding of the response of pebble beds, but also the possibility to characterize the pebbles in a microscopic way. The discrete element method provides promising solutions for pebble bed related problems, such as the quantitative analysis of the crush probability, and moreover the

yield surface of pebble beds. These results strongly support the designing and the optimization of a blanket system on sound theoretical background.

Acknowledgements

This work, supported by the European Communities under the contract of Association between EURATOM and Forschungszentrum Karlsruhe, was carried out within the framework of the European Fusion Development Agreement. The views and opinions expressed herein do not necessarily reflect those of the European Commission. The authors would like to thank Dr. H. Riesch-Oppermann for his useful suggestions on the code implementation, and Mr. Saurabh Dixit, at IIT Kanpur, for his support on the visualization software for DEM.

References

An, Z., Ying, A., Abdou, M., 2007a. Application of discrete element method to study mechanical behaviors of ceramic breeder pebble beds. Fusion Engineering and Design 82 (15–24), 2233–2238.
An, Z., Ying, A., Abdou, M., 2007b. Numerical characterization of thermo-mechanical performance of breeder pebble beds. Journal of Nuclear Materials 367, 1393–1397.
Antony, S.J., 2000. Evolution of force distribution in three-dimensional granular media. Physical Review E 63 (1), 011302.
Aquaro, D., Zaccari, N., 2005. Pebble bed thermal–mechanical theoretical model—application at the geometry of test blanket module of ITER-FEAT nuclear fusion reactor. Fusion Engineering and Design 75 (9), 903–909.
Aquaro, D., Zaccari, N., 2006. Experimental and numerical analysis on pebble beds used in an ITER Test Module Blanket. Fusion Engineering and Design 81 (1–7), 707–712.
Bicanic, N., 2004. Discrete element methods. In: Stein, E., de Borst, R., Hughes, T.J.R. (Eds.), Encyclopedia of Computational Mechanics, vol. 1. Wiley, New York, pp. 311–337.
Christoffersen, J., Mehrabadi, M.M., Nemat-Nasser, S., 1981. A micromechanical description of granular material behavior. Journal of Applied Mechanics (Transactions of the ASME) 48 (2), 339–344.
Cundall, P.A., Strack, O.D.L., 1979. A discrete numerical model for granular assemblies. Geotechnique 29 (1), 47–65.
Dienst, W., Zimmermann, H., 1988. Investigation of the mechanical-properties of ceramic breeder materials. Journal of Nuclear Materials 155, 476–479.
Gan, Y., Kamlah, M., 2007. Identification of material parameters of a thermo-mechanical model for pebble beds in fusion blankets. Fusion Engineering and Design 82 (2), 189–206.
Gan, Y., Kamlah, M., Reimann, J., 2009. Computer simulation of packing structure in pebble beds. In: The 9th International Symposium on Fusion Nuclear Technology (ISFNT9), Dalian, China.
Gilabert, F.A., Roux, J.N., Castellanos, A., 2007. Computer simulation of model cohesive powders: influence of assembling procedure and contact laws on low consolidation states. Physical Review E 75 (1), 011303.
Goldenberg, C., Goldhirsch, I., 2005. Friction enhances elasticity in granular solids. Nature 435 (7039), 188–191.
Gusev, A.A., 1997. Representative volume element size for elastic composites: a numerical study. Journal of the Mechanics and Physics of Solids 45 (9), 1449–1459.
Gusev, A.A., 2007. Asymptotic back strain approach for estimation of effective properties of multiphase materials. Advanced Engineering Materials 9 (1–2), 117–120.
Herrmann, H.J., Luding, S., 1998. Modeling granular media on the computer. Continuum Mechanics and Thermodynamics 10 (4), 189–231.
Jaeger, H.M., Nagel, S.R., Behringer, R.P., 1996. Granular solids, liquids, and gases. Reviews of Modern Physics 68 (4), 1259–1273.
Jodrey, W.S., Tory, E.M., 1985. Computer simulation of close random packing of equal spheres. Physical Review A 32 (4), 2347–2351.
Johnson, K.L., 1985. Contact Mechanics. Cambridge University Press, Cambridge.
Knitter, R., Alm, B., Roth, G., 2007. Crystallisation and microstructure of lithium orthosilicate pebbles. Journal of Nuclear Materials 367–370 (Part 2), 1387–1392.
Kruggel-Emden, H., Simsek, E., Rickelt, S., Wirtz, S., Scherer, V., 2007. Review and extension of normal force models for the discrete element method. Powder Technology 171 (3), 157–173.
Loebbecke, B., Knitter, R., 2007. Procurement and quality control of Li_4SiO_4 pebbles for testing of breeder unit mock-ups. Technical Report, Fusion No. 311, Forschungszentrum Karlsruhe.
Lu, Z., Ying, A.Y., Abdou, M.A., 2000. Numerical and experimental prediction of the thermomechanical performance of pebble beds for solid breeder blanket. Fusion Engineering and Design 49, 605–611.
Makse, H.A., Johnson, D.L., Schwartz, L.M., 2000. Packing of compressible granular materials. Physical Review Letters 84 (18), 4160.
Marketos, G., Bolton, M.D., 2007. Quantifying the extent of crushing in granular materials: a probability-based predictive method. Journal of the Mechanics and Physics of Solids 55 (10), 2142–2156.
Martin, C.L., 2004. Elasticity, fracture and yielding of cold compacted metal powders. Journal of the Mechanics and Physics of Solids 52 (8), 1691–1717.
Martin, C.L., Bouvard, D., Shima, S., 2003. Study of particle rearrangement during powder compaction by the discrete element method. Journal of the Mechanics and Physics of Solids 51 (4), 667–693.
Mesarovic, S.D., Johnson, K.L., 2000. Adhesive contact of elastic–plastic spheres. Journal of the Mechanics and Physics of Solids 48 (10), 2009–2033.
Nemat-Nasser, S., 2000. A micromechanically-based constitutive model for frictional deformation of granular materials. Journal of the Mechanics and Physics of Solids 48 (6–7), 1541–1563.
Procopio, A.T., Zavaliangos, A., 2005. Simulation of multi-axial compaction of granular media from loose to high relative densities. Journal of the Mechanics and Physics of Solids 53 (7), 1523–1551.
Redanz, P., Fleck, N.A., 2001. The compaction of a random distribution of metal cylinders by the discrete element method. Acta Materialia 49 (20), 4325–4335.
Reimann, J., Boccaccini, L., Enoeda, M., Ying, A.Y., 2002. Thermomechanics of solid breeder and Be pebble bed materials. Fusion Engineering and Design 61 (2), 319–331.
Reimann, J., Knitter, R., Piazza, G., 2005. New compilation of the material data base and the material assessment report. Technical Report, Final report on TW5-TTBB-006-D02.
Reimann, J., Pieritz, R.A., Ferrero, C., Di Michiel, M., Rolli, R., 2008. X-ray tomography investigations on pebble bed structures. Fusion Engineering and Design 83 (7–9), 1326–1330.

Richard, P., Nicodemi, M., Delannay, R., Ribiere, P., Bideau, D., 2005. Slow relaxation and compaction of granular systems. Nature Materials 4 (2), 121–128.
Storakers, B., Fleck, N.A., McMeeking, R.M., 1999. The visco-plastic compaction of composite powders. Journal of the Mechanics and Physics of Solids 47 (4), 785–815.
Swope, W.C., Andersen, H.C., Berens, P.H., Wilson, K.R., 1982. A computer simulation method for the calculation of equilibrium constants for the formation of physical clusters of molecules: application to small water clusters. The Journal of Chemical Physics 76, 637.
Thornton, C., Antony, S.J., 1998. Quasi-static deformation of particulate media. Philosophical Transactions of the Royal Society of London Series A—Mathematical Physical and Engineering Sciences 356 (1747), 2763–2782.
Verlet, L., 1967. Computer " Experiments" on classical fluids. I. Thermodynamical properties of Lennard-Jones molecules. Physical Review 159 (1), 98–103.
Ying, A., Huang, H.L., Abdou, M., 2002. Numerical simulation of ceramic breeder pebble bed thermal creep behavior. Journal of Nuclear Materials 307, 827–831.
Ziegler, J.G., Nichols, N.B., 1993. Optimum settings for automatic controllers. Journal of Dynamic Systems, Measurement, and Control 115 (2B), 220–222.
Zimmermann, H., 1989. Mechanische Eigenschaften von Lithiumsilikaten für Fusionsreaktor-Brutblankets. Technical Report, KfK 4528, Kernforschungszentrum Karlsruhe.